



**HAL**  
open science

# Plasmonic enhancement of amorphous silicon solar photovoltaic cells with hexagonal silver arrays made with nanosphere lithography

C Zhang, J M Pearce, Durdu Ö Güney

► **To cite this version:**

C Zhang, J M Pearce, Durdu Ö Güney. Plasmonic enhancement of amorphous silicon solar photovoltaic cells with hexagonal silver arrays made with nanosphere lithography. *Materials Research Express*, In press. hal-02113482

**HAL Id: hal-02113482**

**<https://hal.science/hal-02113482>**

Submitted on 28 Apr 2019

**HAL** is a multi-disciplinary open access archive for the deposit and dissemination of scientific research documents, whether they are published or not. The documents may come from teaching and research institutions in France or abroad, or from public or private research centers.

L'archive ouverte pluridisciplinaire **HAL**, est destinée au dépôt et à la diffusion de documents scientifiques de niveau recherche, publiés ou non, émanant des établissements d'enseignement et de recherche français ou étrangers, des laboratoires publics ou privés.

# **Plasmonic enhancement of amorphous silicon solar photovoltaic cells with hexagonal silver arrays made with nanosphere lithography**

C. Zhang <sup>1,2</sup>, D. O. Guney <sup>2</sup>, J. M. Pearce <sup>1,2,\*</sup>

1. Department of Materials Science & Engineering, Michigan Technological University, Houghton, MI

2. Department of Electrical & Computer Engineering, Michigan Technological University, Houghton, MI

\* Contact author:

1400 Townsend Drive

Houghton, MI 49931-1295

906-487-1466

[pearce@mtu.edu](mailto:pearce@mtu.edu)

## **Abstract**

Nanosphere lithography (NSL) provides an opportunity for a low-cost and scalable method to optically engineer solar photovoltaic (PV) cells. For PV application, NSL is widely used in rear contact scenarios to excite SPP and/or high order diffractions, however, the top contact scenarios using NSL are rare. In this paper a systematic simulation study is conducted to determine the capability of achieving efficiency enhancement in hydrogenated amorphous silicon (a-Si:H) solar cells using NSL as a top contact plasmonic optical enhancer. The study focuses on triangular prism and sphere arrays as they are the most commonly and easily acquired through direct deposition or low-temperature annealing, respectively. For optical enhancement, a characteristic absorption profile is generated and analyzed to determine the effects of size, shape and spacing of plasmonic structures compared to an un-enhanced reference cell. The factors affecting NSL-enhanced PV performance include absorption, shielding effects, diffraction, and scattering. In the triangular prism array, parasitic absorption of the silver particles proves to be problematic, and although it can be alleviated by increasing the particle spacing, no useful enhancement was observed in the triangular prism arrays that were simulated. Sphere arrays, on the other hand, have broad scattering cross-sections that create useful scattering fields at several sizes and spacing intervals. For the simulated sphere arrays the highest enhancement found was 7.4%, which was fabricated with a 250nm radius nanosphere and a 50nm silver thickness, followed by annealing in inert gas. These results are promising and provide a path towards the commercialization of plasmonic a-Si:H solar cells using NSL fabrication techniques.

**Keywords:** amorphous silicon; hydrogenated amorphous silicon; silver; plasmonic; hexagonal array; photovoltaic

## 1. Introduction

Hydrogenated amorphous silicon (a-Si:H) solar photovoltaic (PV) cells provide an inexpensive alternative to bulk crystalline silicon (c-Si) cells [1,2]. Compared to c-Si cells, whose thickness ranges from ten to hundreds of microns, the high absorption coefficient of amorphous silicon enables a-Si:H PV to absorb sufficient solar radiation at submicron level [1,2]. Although material costs are reduced, a-Si:H cell efficiencies are lower as the material suffers from high defect density and short minority carrier diffusion length [3]. Additionally, a-Si:H has light induced degradation known as the Staebler-Wronski Effect (SWE) [4–6], which is dependent on the thickness of the absorber material (i-layer) in an a-Si:H device. Light trapping mechanisms are necessary to assist in alleviating both of these challenges and several forms of optical enhancement have been used in the past [7,8].

One common approach is to introduce a textured anti-reflection surface, which inevitably increases the amount of surface defects, hence increasing recombination sites [9,10]. In order to avoid this deficiency, surface plasmonic nanostructures provide a promising approach to enhancing optical absorption in thin film solar cells and have therefore been investigated [11,12]. Top contact optical enhancement methods have an advantage in terms of fabrication simplicity and avoidance of the substrate effect from the protocrystalline nature of Si:H [13,14] that introduces defects in the i-layer. Many studies have shown the benefits of the light trapping effect through top metallic scatterers [15–17]. In addition, if the metal is made up of nanoparticles, they not only behave as light scatterers but also enable light trapping through high order diffraction [18,19], Fabry-Perot resonance [20], and decrease the top contact sheet resistance.

Although the advantages of plasmonic structures have been well investigated, no plasmonic-based a-Si:H solar cell has been commercialized due to two primary reasons: 1) the effect was demonstrated on unrealistically thin solar cells [21] that if scaled demanded an ultra-thin transparent conducting oxide [22,23] and 2) current fabrication constraints. Recently, work on ultra-thin TCOs has been successful [22], which provides the potential to use this approach on full solar cells. However, traditional fabrication techniques, such as e-beam lithography and focused ion beam, are cumbersome, expensive and difficult to scale up, therefore making them improbable for industry level fabrication. Nanosphere lithography (NSL), however, provides a low-cost scalable technique: by self-assembly, NSL creates size- and shape-controllable colloidal masks, which ease the fabrication of plasmonic patterns via common evaporation or sputtering tools. Depending on the techniques and procedures, patterns like triangular prism [24], rod [25], cylinder [26,27], ring [25,28] or dot [24,25] are developed and their size and spacing can be tuned by selecting appropriately sized spheres.

Previous work provides an opportunity to use NSL for light management on the front surface of a commercial a-Si:H PV cell. Van Duyne et al. completed extensive research on the optical properties of NSL-fabricated plasmonic arrays [24] and Moraescu et al. studied the localized surface plasmon in gold triangular array for sensing applications [29]. For PV application, NSL is widely used in rear contact scenarios to excite SPP and/or high order diffractions [30–33]. However, the top contact scenarios using NSL are rarely found in literature. Giulia et al. report

on a conceptual cells with the capability of 88% absorption using a tapered triangular prism nanoarray for a metal-insulator-metal structure [34]. The discovery, although using a conceptual solar cell, inspired the study of using NSL in top contact scenarios for thin film solar cells.

Here a systematic simulation study is conducted to determine the capability of achieving efficiency enhancement in a-Si:H solar cells using NSL as a top contact plasmonic optical enhancer. The study focuses on triangular prism and sphere arrays as they are the most commonly and easily acquired through direct deposition or low-temperature annealing, respectively. Other patterns such as cylinders, rings or bowls require additional processing and/or equipment that is cost efficient for commercialization. The reference cell to be employed has the same structure without the presence of the plasmonic nanoparticles. For optical enhancement, a characteristic absorption profile is generated and analyzed to determine the effects of size, shape and spacing of plasmonic structures. Conclusions are drawn to validate the feasibility of fabricating commercial cells with this low-cost, widely-accessible, and easily-scalable method.

## 2. Background: Surface plasmon induced scattering

For top contact plasmonic-enhanced PV, the mechanism that contributes to the optical enhancement is forward scattering where the electric field of the incoming plane wave excites a collective oscillation of free electrons in the conduction band in a metal particle, causing re-radiation of light from the metal particle's surface. For particles of subwavelength dimension, the solutions to Maxwell's equation transits from the Rayleigh model to the Mie model [35]. According to Mie's theory, two important physical quantities can be obtained: the scattering and absorption cross-sections, which are defined as the net energy rate of scattering radiation and absorption divided by the incident irradiance. For the scattering field emitted from a dipole moment, the scattering and absorption cross-sections can be expressed as [35]:

$$\sigma_{sc} = \frac{8}{3} \pi a^2 q^4 \left| \frac{\frac{\epsilon_p}{\epsilon_m} - 1}{\frac{\epsilon_p}{\epsilon_m} + 2} \right|^2 \quad (1)$$

$$\sigma_{abs} = 4\pi a^2 q \text{Im} \left[ \frac{\frac{\epsilon_p}{\epsilon_m} - 1}{\frac{\epsilon_p}{\epsilon_m} + 2} \right] \quad (2)$$

where  $\epsilon_p$  and  $\epsilon_m$  are the relative dielectric functions of a metal particle and the medium respectively,  $a$  is the radius of the particle and  $q$  is a dimensionless quantity equaling  $ka$ ,  $k$  is the wave vector in the medium. From the equation it can be seen that surface plasmon resonance occurs when  $\epsilon_p = -2\epsilon_m$ , at which both the scattering and absorption cross-sections exceed the geometrical cross section. Thus, full extinction of the incoming light can be achieved with a fraction of surface coverage. A typical silver nanoparticle with a diameter of 90nm creates a scattering cross-section 10 times larger than that of the geometry cross-section. In addition to dipole modes, radiation damping and dynamic depolarization in large particles break down the quasi-static approximation and enable higher order modes to exist [36,37]. Akimov et al.

discovered the separation of scattering and absorption induced by high order modes, which makes them advantageous in thin-film solar cell applications [38].

Surface plasmon resonance is significantly influenced by particle size, shape and the surrounding environment. For PV applications, the ideal resonance covers a broad range of the spectrum where the photo-active material absorbs most of the radiation (in a-Si:H based PV this is the i-layer). In addition to the scattering cross-section, the corresponding absorption cross-section should be attenuated to avoid absorption competition with the photo-active material. Those are the two principles in designing a plasmonic-enhanced cell. However, NSL has its limitations in pattern creation. With nanospheres of a fixed size, the close packed hexagonal array pattern is the only pattern available. Efforts have been made to extend the diversity of geometric patterns through NSL using multilayers [24], non-close packed arrays [39,40], and non-hexagonal symmetries [40]. However, literature rarely reports applications of these novel structures, largely due to the difficulty in uniformly replicating these structures, particularly over large areas.

In this study, two of the most common structures from NSL are investigated and the results compared for the 1) nano-triangular prism array by direct deposition through a colloidal mask and 2) the nanosphere array following the gentle annealing of the nano-triangular prisms. These approaches do not require sophisticated equipment or processing. They are both stable, provide high yield products and are straight forward to scale up at low-cost, meeting the industrial requirements for commercial solar cells.

## **2. Methods**

The simulation is carried out using COMSOL Multiphysics 5.1 with the RF module package, which is based on finite element methods (FEM). The scattering cross-section study and solar cell performance analysis are performed separately with different setups, as described below.

### **2.1 Cross section model**

Simulation work for cross-section analysis is based on a single scatterer where the interaction with scattered fields from other scatterers are neglected. The isolation is necessary in order to obtain an accurate calculation of the cross-sections. The interactions between the scatterers are included in the cell simulation in which the array of scatterers is taken into account. Models for the triangular prism and sphere cross-section analysis are shown in Fig 1 a and b, respectively. Silver nano-triangular prisms/spheres sit at a square center, the top and bottom half of the model are air and ITO, each with a thickness of 750nm to provide a far enough space for the scattered and incident fields to propagate. To represent a real cell environment, the ITO used in the simulation has the same optical parameters as the one used in the reference cell. The definition of triangular prism dimensions is shown in Fig 2. The three enclosing nanospheres of radius  $R$  specify the triangular prism geometry. The tips of the triangular prisms are filleted to avoid numerical errors around the sharp tips. The spheres are annealed triangular prisms whose volume is assumed to be constant during the shape transformation, therefore the spheres are specified by and compared with their triangular prism counterparts. The whole structure is enclosed by a 150nm thick, perfectly matching layer to absorb all propagating and evanescent waves. Incident

plane waves of intensity  $I_0$  and polarization in the y-direction are excited through the port setup. The scattering and absorption cross-sections are derived from the following equations:

$$\sigma_{sc} = \frac{\oiint \mathbf{P}_{sc} \cdot \mathbf{n} dS}{I_0} \quad (3)$$

$$\sigma_{abs} = \frac{\iiint Q_{loss} dV}{I_0} \quad (4)$$

where  $dS$  and  $dV$  are the differential surface area and differential volume of the nanoparticle, respectively.  $P_{sc}$  is the Poynting vector of the scattered field,  $\mathbf{n}$  is the unit vector normal to the particle surface, and  $Q_{loss}$  is the power density lost in nanoparticle.

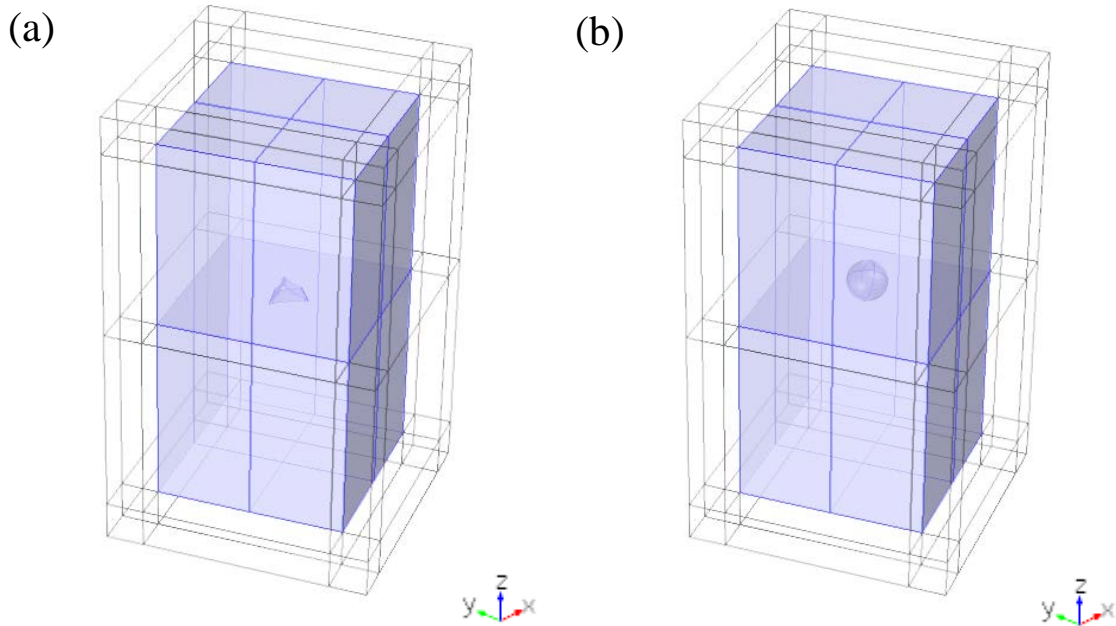


Fig. 1 Models of a single scatterer: silver triangular prism (a) and silver sphere (b), shaded domains are physical entities, transparent domains are perfectly matching layers (PMLs).

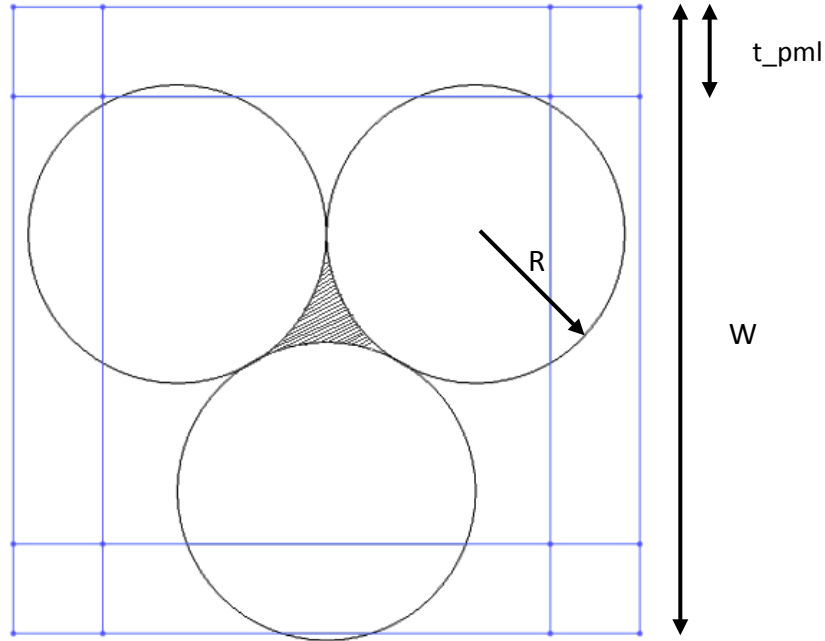


Fig 2. 2D top view of triangular prism model, silver triangular prism dimension is defined by the grey shaded area surrounded by three masking nanospheres with radius  $R$ .  $W$  is the length of the unit cell,  $t_{pml}$  is the thickness of the PMLs. The triangular prism tips are tapered to reflect the real triangular prisms produced in fabrication, as well as to avoid numerical errors around the narrow regions in simulation.

## 2.2 Solar cell model

The reference cell employed, shown in Fig. 3, consists of 200nm silver and 100nm aluminum doped zinc oxide (AZO) as the back contact, followed by n-, i-, and p-type hydrogenated amorphous silicon (a-Si:H) photo-active layers with thicknesses of 22.4nm, 350.5nm, and 17.5nm, respectively. A 36nm optimized indium tin oxide layer [22] serves as the top contact, which is thinner than common commercial PV cells in order to be able to use plasmonic enhancement. Dielectric functions of the p-, i-, and n-type a-Si:H, AZO and ITO are measured in J.A. Woolam's variable-angle spectroscopic ellipsometer, and the silver data is acquired from S. Babar [41].

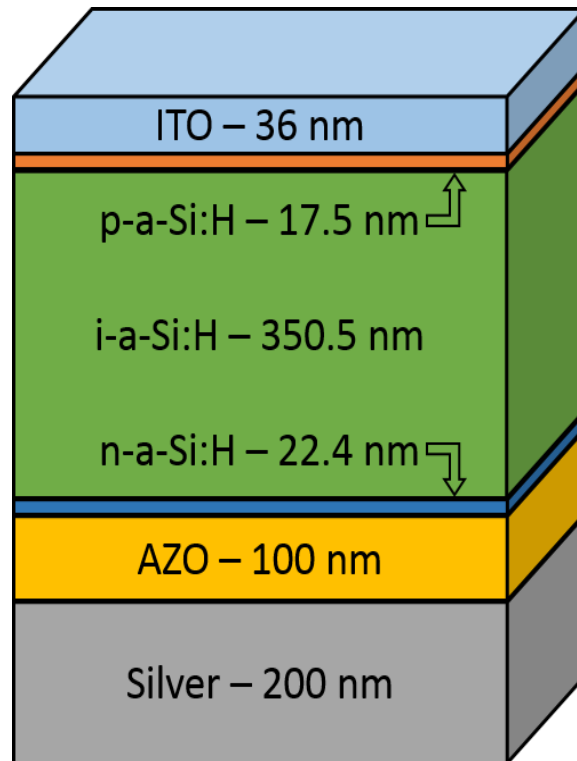


Fig 3. Reference solar cell structure.

Given the dielectric functions and geometry constants of each layer, the method solves for the full Maxwellian equations in a constrained range of the solar spectrum where a-Si:H is active (300nm to 750nm). Periodic boundary conditions are applied to include interactions between nanoparticles as an array, and also to help reduce the computation resource usage due to lattice symmetry. Electromagnetic waves polarized in the y-direction are sent through a port on top of the structure. PML layers sandwich the cell to absorb escaping waves. The model has included all major optical processes occurring in the structure and is hence very close to real situation. The simulation models are described in Fig. 4.

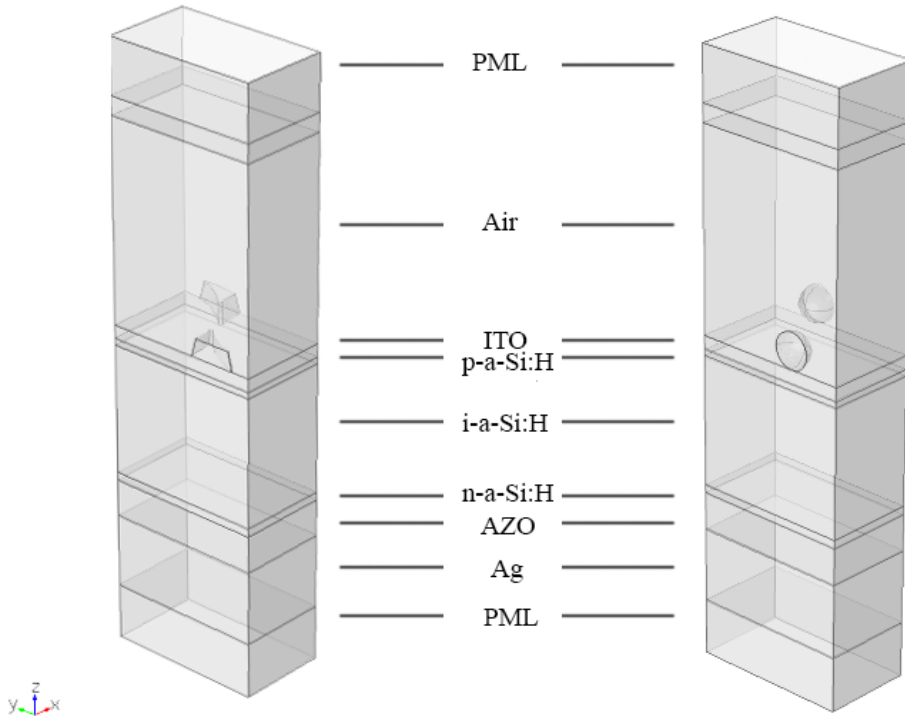


Fig. 4. Models of a-Si:H solar cell with a silver triangular prism (left) and a silver sphere (right), layers from bottom to top are PML (150nm), silver (200nm), AZO (100nm), n-a-Si:H (22.4nm), i-a-Si:H (350.5nm), p-a-Si:H (17.5nm), ITO (36nm), silver particles (various sizes) and air (thickness = 2x wavelength). PEM and PMC boundary conditions are applied on four sides to reduce the computation domain to its  $\frac{1}{4}$ .

The power loss densities in each layer are integrated over their volumes to obtain a global absorption profile. The integrated absorption in the i-layer over the AM 1.5 solar spectrum is employed as the standard in the study for cell performance measurement and comparison, as seen in the equation below:

$$P = \int A(\lambda)Q_{AM1.5}(\lambda)d\lambda \quad (5)$$

$P$  is the absorbed power density,  $A$  is the ratio of absorbed power to incident power,  $Q_{AM1.5}$  is the solar irradiance spectrum, and air mass = 1.5, obtained from the National Renewable Energy Laboratory (NREL)[42].

### 3. Results and Discussion

Scattering cross-sections of single triangular prism and sphere scatterers are illustrated in Fig. 5(a-d). The shaded area is the photo-active region of a-Si:H and the scattering falling in this region will be advantageous in plasmonic enhancement. The triangular prism spectrums show two well-separated peaks. The two peaks are associated with two localized surface plasmonic

resonance (LSPR) modes – the first order dipole mode ( $l=1$ ) at longer wavelengths, and the second order quadrupole mode ( $l=2$ ) at shorter wavelengths. The simulations agree with previously established experimental results [29]. Both peaks are subjected to broadening and red-shifts as the nanosphere size increases. Dipole peaks are more sensitive to size changes and move faster towards infrared, leading to scattering outside the a-Si:H photo-active region (Fig 5.a). The quadrupole peak is weak in shadow triangular prisms and grows fast as the thickness increases. In Fig 5. b, a weak peak occurs at 380nm and red-shifts slightly with the triangular prism thickness, which can be attributed to resonance at higher ( $l>2$ ). The peak overlaps and merges with its quadrupole neighbor in thicker triangular prisms. High order modes are considered a result of inhomogeneous polarization and are normally seen in larger particles [43]. When the triangle height increases to be comparable to the incident light wavelength, the incident light cannot polarize the triangular prism within constant phase, this inhomogeneous polarization leads to an electric field gradient in the triangular prism and consequently, significant retardation of the resonance allows high order modes to arise and even dominate the dipolar resonance when  $h=200\text{nm}$  in  $R=350\text{nm}$ . In Fig. 5b there is a tendency for the quadrupolar and dipolar mode resonance peaks to overlap each other as the thickness of the triangular prism increases. The interferences between the quadrupole and dipole may give rise to Fano resonance, which can be tuned to maximize forward light scattering and benefit a-Si:H absorption [44].

Cross-section profiles of sphere silver scatterer have been widely studied and discussed. For PV applications, sphere particles are preferred over triangular prisms due to the larger, broad-spectrum scattering cross-sections of the sphere. More importantly, for a-Si:H, scattering cross-sections stemmed from spheres have better spectral coverage in the photo-active region. Unlike triangular prisms, spheres are geometrically isotropic and therefore do not have well-separated resonance peaks. Dipole resonance overlaps with high order peaks to provide broader peaks from 340nm to 800nm for larger particles (Fig. 5. c. d). As the sphere size increases, the separation of the resonance peaks becomes noticeable; for example, in Fig. 5 d, in the  $h=200\text{nm}$  group, the dipole, quadrupole, and octupole peaks are at 520nm, 460nm and 400nm respectively. As with the triangular prisms, the scattering cross-section red-shifts and becomes stronger with the particle sizes. As pointed by Akimov, higher order modes can contribute significantly to thin-film cells by maximizing the scattering within while leaving the absorption peak outside the photo-active region [38]. Theoretically, NSL allows the creation of sphere particles of any size. This makes the method extremely useful in PV applications as one can tune the scattering peak to be within the spectrum where absorption is weak due to poorly trapped light.

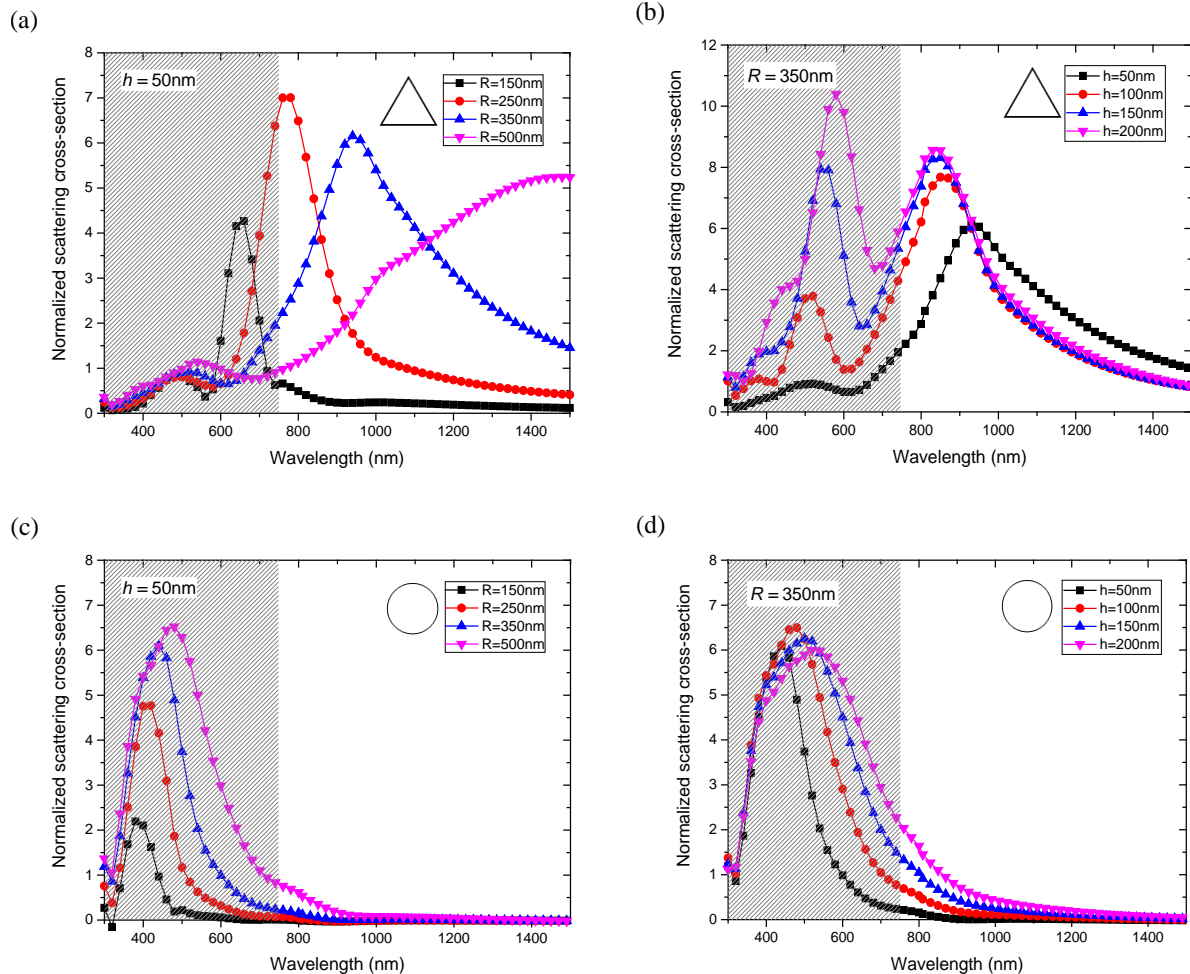


Fig 5. Scattering cross-sections of silver triangular prisms (a and b) and spheres (c and d) scatterer.  $R$  is the radius of nanospheres in NSL and  $h$  is the deposited silver thickness. The metrics apply to the sphere array under the assumption that the volume of the plasmonic nanoparticles is not changed during annealing.

The optical absorption rates of the  $i$ -layers of the modeled nanoparticle enhanced plasmonic cells are shown in Fig. 6 ( $R=250\text{nm}$ ,  $h=50\text{nm}$ ). The reference cell's  $i$ -layer absorption rate is also shown for comparison. The interaction between the incident light and silver nanoparticles on top of the cell is complicated, and therefore the absorption in silver nanoparticles is also shown in Fig. 6 to better illustrate this interaction.

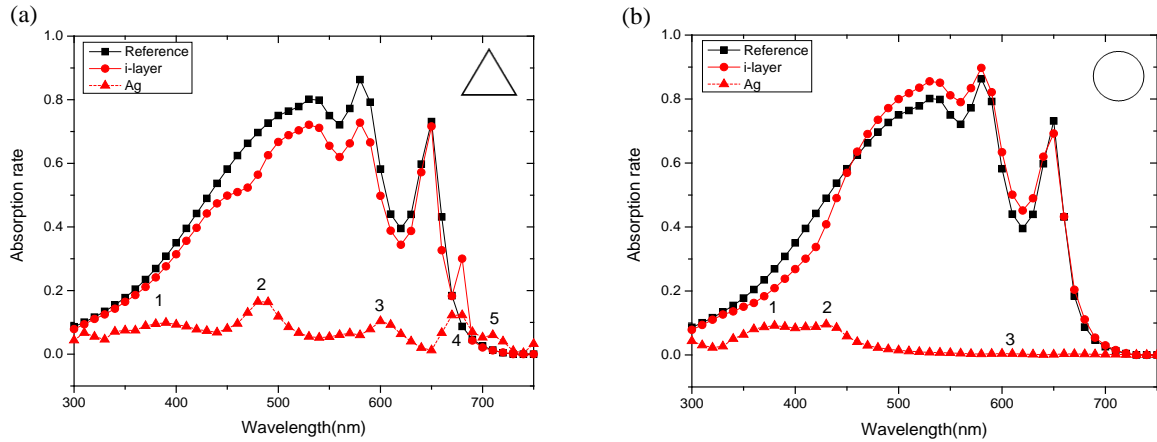


Fig.6. Absorption profile of the i-layer for the triangular prisms (a) silver nanoparticles array and sphere (b) silver nanoparticles array, assembled by NSL ( $R=250\text{nm}$ ,  $h=50\text{nm}$ )

The absorption profile in the i-layer for the triangular prism array shows an overall scaling-down compared to the reference profile, clearly indicating that a triangular prism array of this geometry damages cell performance. A triangular prism array of this size and geometry is not able to provide a strong scattered field into the i-layer because the dipole scattering cross-section peak is out of the active wavelength range, hence there is not a significant scattering effect to increase absorption in the i-layer at relevant wavelengths for PV. While high order scattering falls in the active spectral regions, however, the scattering that stems from high order resonance is weak (Fig. 6 (a,b)) and not well-separated from the corresponding absorption, which competes with the i-layer and hence negatively contributes to optical enhancement. The high absorption rate in triangular prism nanoparticles can be attributed to their anisotropic geometry, which concentrates and dissipates energy at the triangular prism tips. To characterize the near field effect and explore the room for optimization, the absorption profiles of the triangular prism nanoparticles was studied. Five absorption peaks are identified at 390nm 490nm, 600nm, 680nm and 710nm (Fig. 6. (a)), with the plotted field distribution in the xy- and yz-planes corresponding to each peak, as shown in Fig. 7.

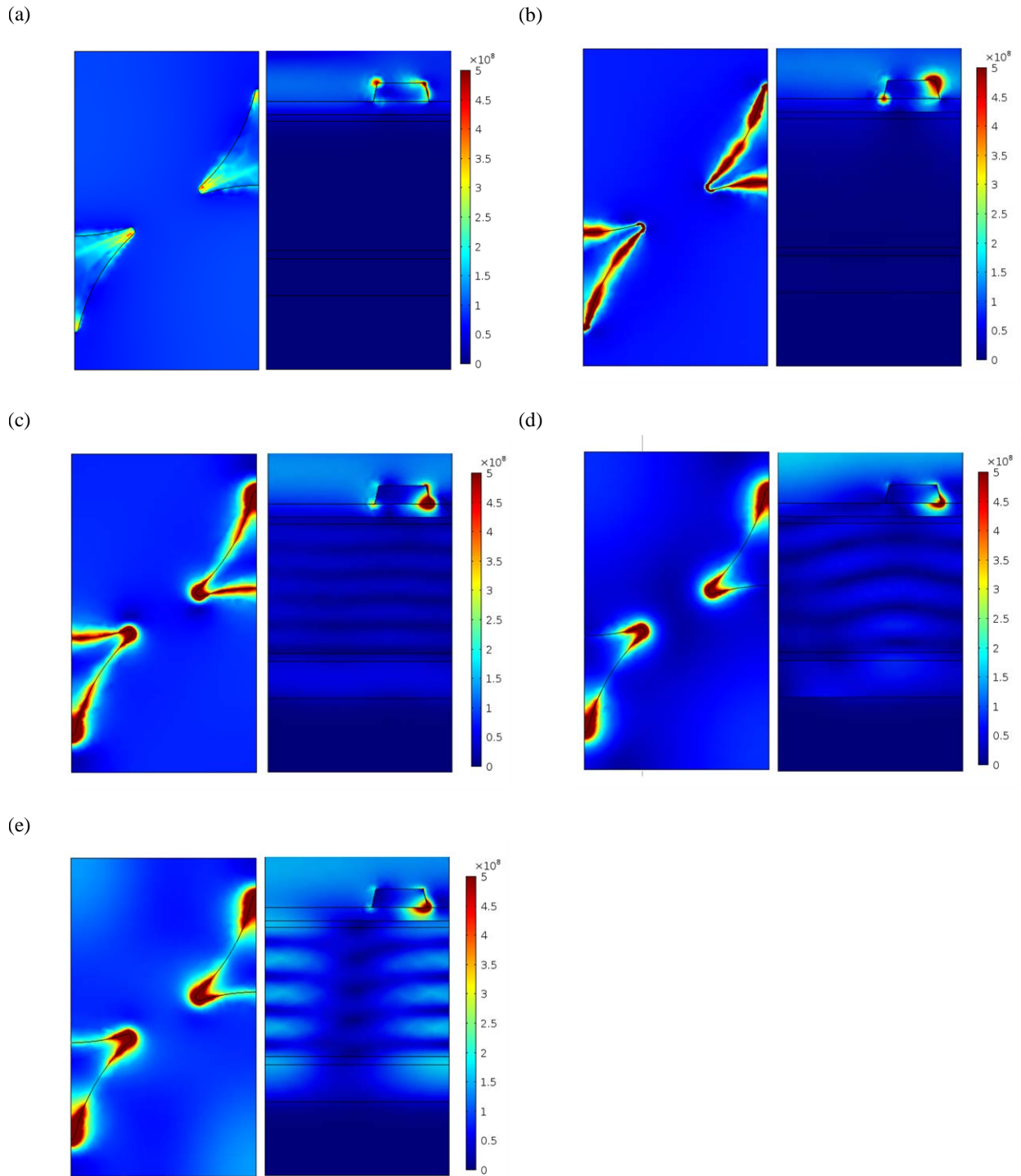


Fig. 7 Silver triangular prism array electric field normal mapping at 390nm, 490nm, 600nm, 680nm, 710nm (a-e). The mapping is drawn at the xy-plane ( $z=z_{\text{triangle\_base}}$ ) and the yz-plane ( $x=0$ ), shown to the left and right respectively for each subset. Incident wave polarization in the y-direction

In Fig. 7 a) and b), the field distribution across the triangular prisms is found to be along the edges of the particle, whereas the distribution in c), d) and e) is mainly concentrated on the tips. This concentration process becomes more prominent with different wavelengths. According to a recent study by Herr et al. the near-field enhancement ( $E/E_0$ ) can reach up to 80 at the triangular prism bowtie gaps [45]. In the  $yz$ -plane mapping, the distribution of the enhanced electric field is highly discrete, with multiple hot spots arising around the corners of the triangular prism. As previously discussed, the dipolar mode of triangular prisms of this size occurs at 800nm, which is out of the spectrum being considered. The emergence of multiple absorption peaks comes from the high order modes and the interactions between them. Due to broken symmetry and the excitation of high order modes, a non-linear optical process and a second harmonious emission can occur at lower wavelengths [46]. Fig. 7 a) and b) shows that the enhancement of the near field tends to selectively reside on the edges, a typical sign of retardation, in which only a fraction of the triangular prism experiences the polarization [47]. In the red region of the electromagnetic spectrum, the enhanced near field is concentrated at the tips, which is more dipolar-like. Due to the blocking ITO layer and low carrier life time in the p-layer, the i-layer does not benefit from the near field enhancement; on the contrary, the excitation of those modes causes strong energy dissipation within the triangular prism. Consequently the triangular prism array is not an ideal scatterer for a-Si:H cells. It is worth noticing that in Fig. 7, d) and e), the plasmonic resonance, coupled into the waveguide mode, leads to high order diffraction modes propagating within the i-layer. The small peak at 680nm confirms this analysis. The diffraction that occurs at 710nm is close to the absorption limit of a-Si:H, and the contribution to the enhancement is therefore negligible.

For sphere hexagonal arrays ( $R=250\text{nm}$ ,  $h=50\text{nm}$ ), three silver absorption peaks are identified at 380nm, 430nm 610nm, corresponding to octupole, quadrupole and dipole resonances respectively. Absorption in dipolar resonance contributes less than 1% of the total absorption, from Equation 1 and 2, and its corresponding scattering cross-section can be many fold greater than the absorption cross-section, which boosts a-Si:H absorption at longer wavelengths. The increase in i-layer absorption around 610nm supports this analysis. With the high order modes, resonance can be both beneficial and detrimental. The field distribution snapshot at the  $xy$ -plane ( $Z=Z_{\text{sphere\_center}}$ ) and the  $yz$ -plane ( $x=0$ ) were taken and shown in Fig. 8(a-c).

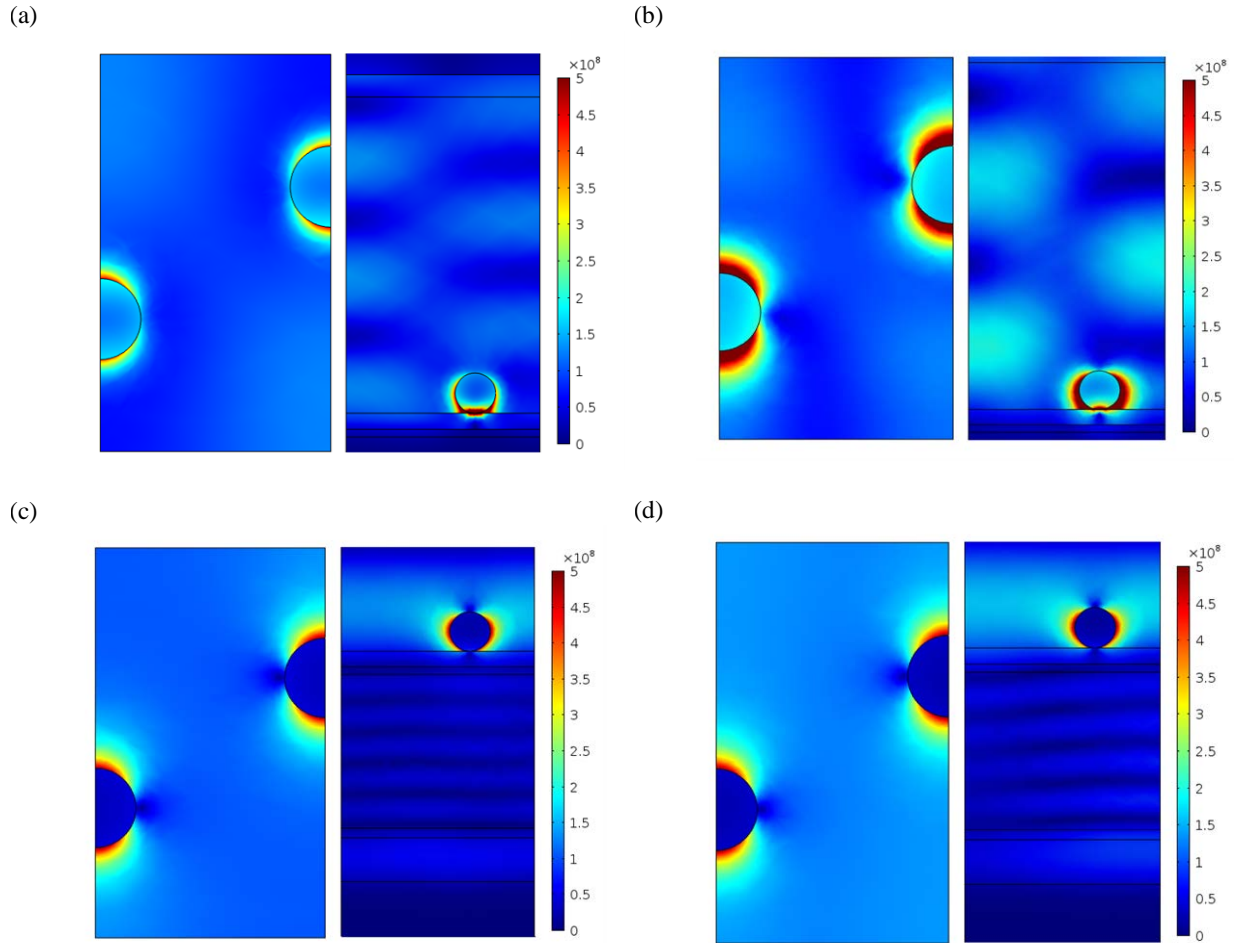


Fig. 8 Silver sphere array electric field normal mapping at 380nm, 430nm, 610nm and 680nm (a-d). The mapping is drawn at xy-plane ( $z=z_{\text{sphere\_center}}$ ) and yz-plane ( $x=0$ ), shown to the left and right respectively for each subset. Incident wave polarization in y-direction. Sphere array fabricated by NSL using a nanosphere radius of  $R = 250\text{nm}$ , with deposited silver thickness  $h = 50\text{nm}$ .

As previously discussed, the separation of absorption and scattering in multiresonance modes can be beneficial if they are engineered to be absorptive outside the a-Si:H active region while scattering inside that region. However, to achieve this with NSL is difficult since the latter offers limited options in engineering the inter-particle spacing. In this case, the enhancement from 450nm to 580nm is gained from the useful scattering originated from both dipolar and higher order modes resonance. The drawback at  $<450\text{nm}$  region is a consequence of high order modes absorption, where the enhancement becomes negative. Field distribution shows that the backward scattering/diffraction also causes the losses. Plasmonic coupling of incident light results in strong backward diffraction at both 380nm and 430nm (Fig. 9 (a,b)). Useful diffraction found at 680nm gives rise to a small bump in the i-layer absorption profile (Fig. 9 d), but this is not as strong as the diffraction caused by triangular prism array at the same wavelength.

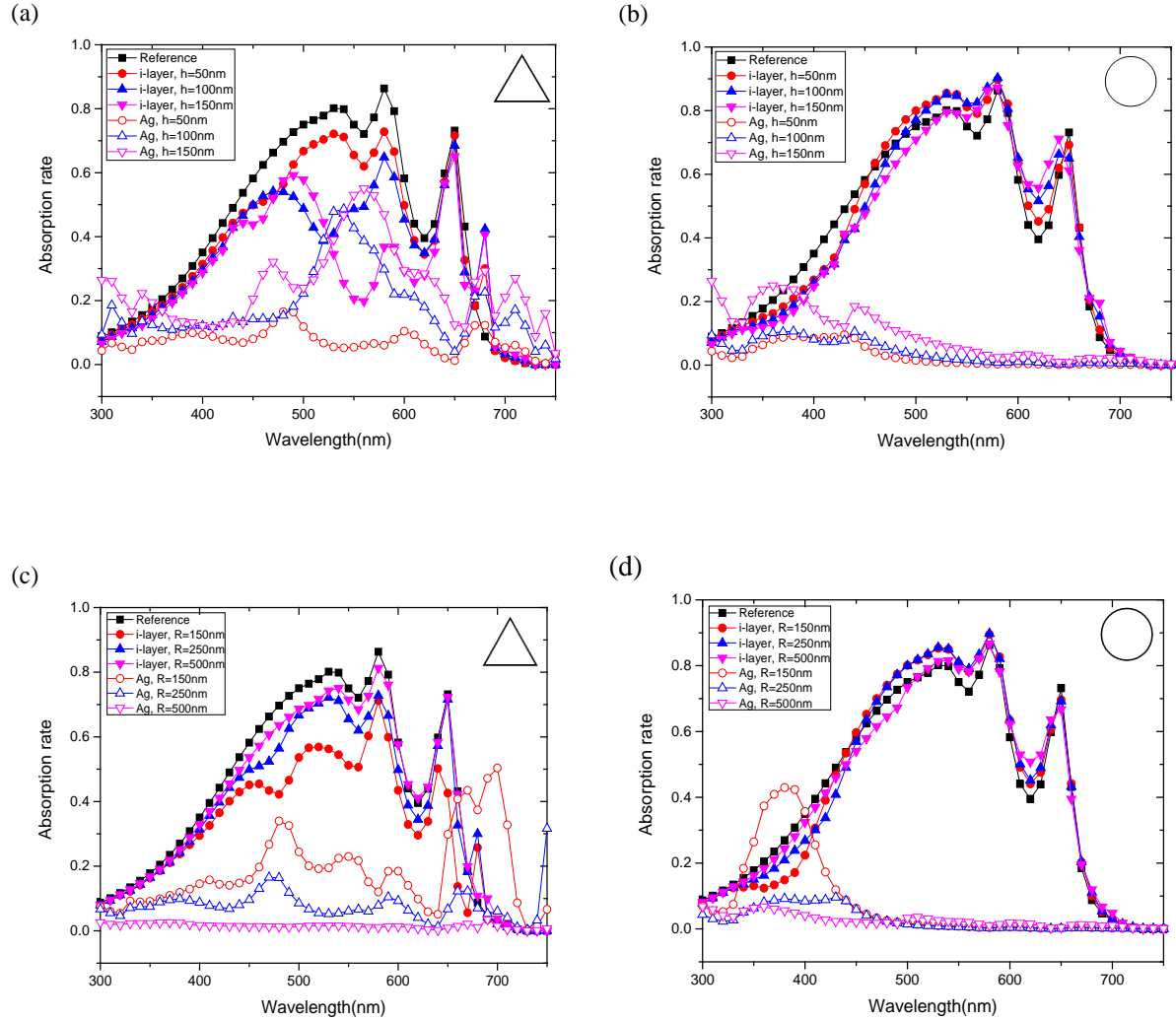


Fig. 9. Absorption profile of the i-layer and silver nanoparticles for triangular prism (a,c) and sphere (b,d) arrays at  $R=250\text{nm}$  (a,b) and  $h=50\text{nm}$  (c,d)

Fig. 9. shows the changes in the absorption profile as  $R$  and  $h$  vary. The behavior in the triangular prism array case is complicated and none of the results so far show a promising enhancement, compromising the cell performance rather than boosting it. Fig. 9 (a) shows the spectral sensitivity of the silver particle absorption. As can be seen in Fig. 9a, there are three major high order absorption peaks that red-shift with the increasing thickness as they all grow in strength. Those not red-shifted are newly emerged peaks as the thickness increases. A greater thickness appears to require longer wavelengths of the incident wave to interact with the entire triangular prism structure, and the chances of creating an electric field gradient along the triangular prism pillar also increases, hence increasing the retardation effect. This explains the stronger, red-shifted higher order absorption peaks. The scattered field induced by high order resonance, though showing a significant increase from previous analysis, still cannot compete with the absorption. In addition to thickness, increases in  $R$  have the opposite effect: absorption peaks are pushed slightly towards red and the fraction of energy absorbed by particles is reduced significantly. For instance, the absorption profile of the triangular prism with  $R=500\text{nm}$ ,

$h=50\text{nm}$  is nearly a flat line, with only weakly observable peaks. Although the corresponding i-layer absorption increases, this increase is not sufficiently significant to show enhancement when compared to the reference cell. The reason for this could be the increased reflection caused by larger triangular prisms, which behave more like mirrors that reflect light out of the cell rather than scatter light into it. A closer analysis of the absorption rate shows the complementary characteristics between the i-layer and the nanoparticles, indicating that the absorption of nanoparticles is the main source of performance degradation. In the worst case scenario, the triangular prism array delivers an enhancement of -43% at  $R=250\text{nm}$ ,  $h=150\text{nm}$ . The diffraction peak is subject to system symmetry and is hence located at  $680\text{nm}$  regardless of triangular prism dimensions. The intensity of this peak, however, relies on the coupling of the plasmonic resonance in the nanoparticle, and it can therefore fluctuate with geometry, as observed in Fig. 9 a,c. In this series, the diffraction peaks are generally not strong enough to compensate the losses from the parasitic absorption in the triangular prisms. More importantly, both solar irradiance and a-Si:H absorption are weaker at  $680\text{nm}$ , therefore limiting the benefit from diffraction .

The sphere arrays show similar profiles as discussed for the  $R=250\text{nm}$ ,  $h=50\text{nm}$  case. The sphere size is expressed in  $R$  and  $h$  for fabrication convenience, bearing in mind that the  $R$  and  $h$  themselves do not directly represent the sphere size, which is a result from annealing a triangular prism fabricated using  $R$  and  $h$  metrics. In the sphere cases, both  $R$  and  $h$  control the size, with  $R$  additionally also governing inter-particle spacing. The previous discussion has shown that large particles deliver more scattered light by supporting the excitation in high order modes. It is also observed that larger sphere sizes generally result in better overall optical enhancement (Fig. 9, b). The sphere sizes should not be too large, however, or they will shield the a-Si:H underneath from sunlight. The sphere spacing is also important, as can be seen in Fig. 9, d, where the absorption peak is significantly raised when the spheres are close to each other. The consequence of this is a decrease in the i-layer absorption at the same wavelength range. A well-separated sphere array shows mild absorption in high order absorption profiles despite an increased radius (Fig. 9,d). Nevertheless, the overall influence of the nanoparticles is complicated, and trade-offs occur between better scattering and a lower shielding effects, leading to the optimization for  $R$  and  $h$ . It should also be noted that the diffraction peak in the sphere array is much weaker compared to its equivalent triangular prism array. One explanation of this phenomenon is that the support from surface plasmon polariton (SPP) spheres as the contact surface is far less when compared to the triangular prisms, resulting in less coupling of the diffraction modes.

NSL-based solar cells allow for two degrees of freedom for optimization: the nanosphere radius  $R$  and the silver film thickness  $h$ . Smaller spheres are created by reducing the silver deposition time while keeping the  $R$  constant. Therefore, in the triangular prism array, the ratio of shaded area to the entire surface is constant and independent of  $R$ , while it can fluctuate with sphere arrays, whose coverage changes with both  $R$  and  $h$ . The optimization is performed to tune both  $h$  and  $R$  to maximize the performance of the solar cell. The absorption rate is integrated into the solar irradiance spectrum (air mass = 1.5) to obtain the optical enhancement, OE. Table. 1 shows the OE of modeled a-Si:H plasmonic-enhanced solar cells.

Table 1. AM1.5 solar irradiance spectra integrated optical enhancement (OE) for triangular prism and sphere arrays fabricated by various  $R$  and  $h$  combos.

$R$ (nm)	$h$ (nm)	OE triangle (%)	OE sphere (%)
<b>150</b>	25	-13.34	4.30
	50	-26.73	6.62
	100	-43.56	3.48
	150	-54.76	-8.75
	200	-60.24	-26.35
<b>200</b>	25	-10.10	4.80
	50	-18.38	7.22
	100	-35.00	3.09
	150	-48.05	-10.34
	200	-57.72	-27.37
<b>250</b>	25	-7.87	4.73
	50	-11.40	7.40
	100	-23.08	4.40
	150	-34.24	-4.86
	200	-43.61	-15.79
<b>300</b>	25	-7.32	4.19
	50	-9.12	3.46
	100	-15.86	-4.12
	150	-23.68	-11.51
	200	-27.19	-17.77
<b>350</b>	25	-6.43	4.71
	50	-7.09	2.88
	100	-11.24	-7.26
	150	-15.02	-14.37
	200	-16.93	-19.52
<b>400</b>	25	-5.73	4.85
	50	-5.76	3.94
	100	-8.00	-6.14
	150	-13.95	-15.47
	200	-17.36	-22.15
<b>450</b>	25	-5.48	4.30
	50	-4.51	4.42
	100	-4.89	-1.00
	150	-10.07	-6.26
	200	-13.96	-10.25
<b>500</b>	25	-5.47	1.88
	50	-4.98	1.50
	100	-4.72	-0.45
	150	-9.01	-2.51
	200	-11.41	-4.57

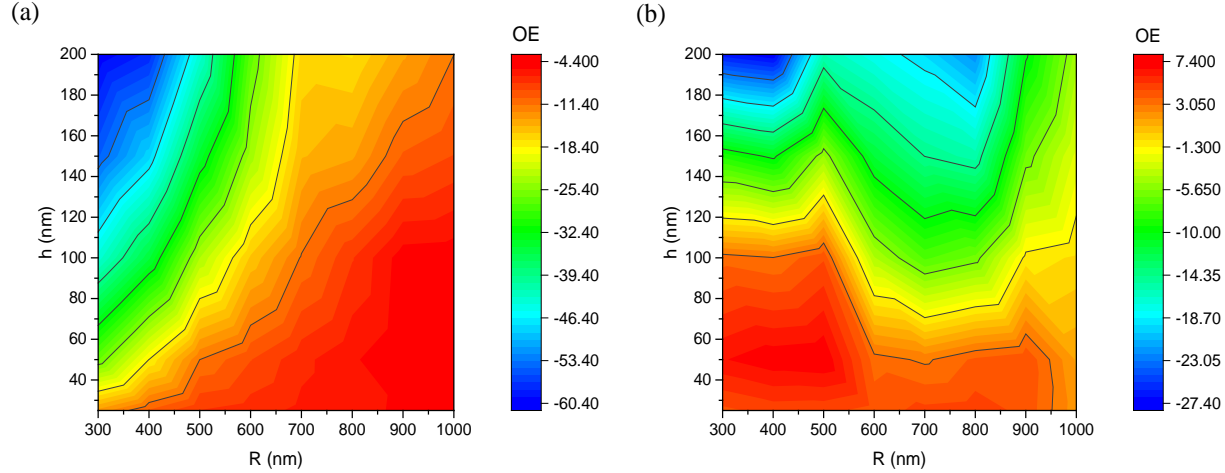


Fig. 10 AM1.5 solar irradiance spectra integrated optical enhancement (OE) contours plot against  $R$  and  $h$  for triangular prism (a) and sphere (b) arrays.

As can be seen in Table 1, there is no positive OE observed for triangular prism arrays with any of the investigated parameters. From previous near field analysis it is clear to see that enhanced field is strongly localized at triangular prism hot spots like edges and tips. The absorption profiles indicate the energy is absorbed and dissipated as heat rather than causing useful diffraction or scattering. The greater the thickness, the larger the surface area that creates hot spots, as can be seen from Fig. 10. a) As such, given the nanosphere radius  $R$ , OE losses increase with the silver film thickness,  $h$ . Simultaneously, at a constant  $h$ , larger nanospheres improve the OE but do not elevate it to above zero. Absorption is drastically reduced when the nanoparticle size becomes comparable to the half-wavelength of light, with resonance peaks moving far to the infrared region and the useful scattering within the photo-active spectral range also being reduced. The large triangular prism array on top of ITO serves as a mirror, shading the cell from incoming sunlight. Hence, even when absorption is not a limiting factor in cell performance, the shading effect still cuts the cell performance. Fig. 10 a) additionally shows that the effective shading is less harmful than the parasitic absorption in nanoparticles, as can be seen in the much more negative OE with the smaller nanospheres. For the sphere array, a useful enhancement of  $\sim 7\%$  is crowded in the bottom-left corner in Fig. 10 b), suggesting that smaller nanospheres with a moderate silver thickness could produce the best results. Silver sphere particles that are too closely packed reduce the OE. This phenomenon could possibly be explained by large shading areas. For  $R = 150\text{nm}$ ,  $h = 200\text{nm}$ , the effective coverage of silver particles reaches 20%, where useful scattering cannot compensate the shading losses. The absorption of the silver spheres rises significantly with larger particles, with  $R = 150\text{nm}$ ,  $h = 200\text{nm}$  the absorption peaks, showing 60% of the energy flux are converted into heat. Destructive interference between scattered fields is another reason for reduced enhancement. In Fig. 8 b), a distorted near field is observed, indicating the excited near fields at the sphere gaps are repelling each other. Although using larger nanospheres lessens this parasitic absorption, the overall enhancement is not as prominent as with smaller nanospheres. To sum it up, the highest OE obtained in this series simulation is 7.4 %, with  $R = 250\text{nm}$ ,  $h = 50\text{nm}$ .

Although there is enhancement with the nano sphere patterned array on a realistic *i*-layer thickness, it is limited and not as great as the percent increase observed in artificially thin plasmonic cells reported in the literature [30,48]. The cell performance here is plagued by the triangular prism absorption, as have been discussed by Sherry et al.[49]. Radiative damping grows significantly with the particle size. For the nano triangular prism arrays with heights smaller than 25nm, the radiative damping is low and not able to compete with scattering, thus the emission dominates over absorption. With increases in particle sizes the absorption rate is comparable to the light emitting rate. As Morarescu added, the aspect ratio of the triangular prisms also plays an important role that affects the localized surface plasmon modes [29]. A good agreement with this observation can be found in Figure 9c. Clearly for the given spectrum range, the absorption is drastically diminished by increasing the aspect ratio. For  $R=500\text{nm}$ ,  $h=50\text{nm}$ , the nano triangular prism absorption profile is flattened to be less than 5 percent throughout the spectrum. The sphere arrays, on the other hand, demonstrate greater capability to scatter light than the triangular prisms. More importantly, the scattering cross-section of sphere spectrally overlaps the a-Si:H absorbing region, the scattered light is more effectively contributes to a-Si:H absorption.

Surface patterning is a balance of art and also the key to access plasmonic enhancement. Although NSL offers scalable and inexpensive fabrication, it comes at the cost that the flexibility of patterning are limited. Hexagonal arrays are the only possible outcome from a naturally close-pack structure, leaving little room to the variation in symmetry. Despite the fact that non-closed packed structures are made available through NSL [50–52], they are not the naturally occurring configuration and thus require additional techniques to assist fabrication, such as employing a template [52]. Those add-on techniques challenges the motivation to keep the low-cost production possible via NSL. Because of the limitation, the enhancement that can be extracted from the structure is not as good as the state-of-art plasmonic a-Si:H cell [30]. However, it does open a gate for plasmonic a-Si:H to be commercialized.

In this study the two conceptual geometries that can be easily accessed from NSL template are modeled to prove the concept of plasmonic enhancement from hexagonal array scatterer. The result shows clearly how geometry difference can influence plasmonic enhancement, and prove that with the same symmetry, particles with irregular shapes are not ideal scatterer for plasmonic application. Nevertheless, NSL is a versatile method supports a variety of other geometries and patterns that is not covered in this research. It is necessary to continue the work with other possible geometries or patterns such as nanocone, nanodots, nanorings, nanopillars which are proved to be NSL-compatible. Moreover, selective etching by RIE is commonly implemented to adjust the nanosphere sizes. By reducing nanosphere sizes, the silver nanoparticles are able to form a connected silver network that greatly improves the top contact conductivity. This could be extremely useful to compensate the poor conductivity in ultra-thin ITO. A thinner ITO with silver nano network that delivers equivalent conductivity can in turn benefit plasmonic scatterer by narrow down the distance to the active layer. Last, the exact anneal geometry of silver nano triangular prism is related to the surface wettability and surface tension of silver on ITO, which can vary with the ITO quality. Experimental work is required to validates the geometry and prove the enhancement.

## 5. Conclusions

In this study, the plasmonic effect of triangular prism and sphere silver nano arrays fabricated using NSL techniques have been studied in detail on a-Si:H solar cells. Scattering from the silver triangular prism and sphere arrays deposited on top of conducting ITO layer produce completely different cross-section profiles. Well-separated resonant modes are identified in triangular prism arrays, with substantial red-shifts found as the triangular prism spacing increases. At the same time, the thickness of the silver film tends to overlap two primary resonance peaks into a broad peak when increased to above 200nm. Scattering from higher order modes increases substantially with greater silver thickness, whereas dipole peaks are less affected. Cross-sections in sphere arrays show a continuous, broad peak across the main absorbing spectrum from 300nm to 700nm, and the peaks further extend to infrared as the spheres become larger. The broad scattering cross-section peak observed is a combination of multiple resonance modes that are not well-separated at the UV-visible range. For solar photovoltaic applications, the sphere arrays are more beneficial when generating broad scattering peaks than their simulated triangular prism array counterparts.

Plasmonic-assisted cell performance has been investigated in numerous simulations. The factors affecting cell performance include absorption, the shielding effect, diffraction, and scattering. In the triangular prism array, the parasitic absorption of the silver particles proves to be problematic, and although it can be alleviated by increasing the particle spacing, no useful enhancement was observed in the triangular prism arrays that were simulated. Sphere arrays, on the other hand, can be engineered to be advantageous to PV performance. Broad scattering cross-sections from the spherical particles create useful scattering fields at certain sizes and spacing. For the simulated sphere arrays the highest enhancement found was 7.4%, which was fabricated with a 250nm radius nanosphere and a 50nm silver thickness, followed by annealing in inert gas. These results are promising and provide a path towards the commercialization of plasmonic a-Si:H solar cells using cheap and scalable NSL fabrication techniques.

## 6. Acknowledgements

This work was supported by the National Science Foundation under grant award number CBET-1235750.

## 7. References

- [1] D.E. Carlson, C.R. Wronski, Amorphous silicon solar cell, *Appl. Phys. Lett.* 28 (1976) 671. doi:10.1063/1.88617.
- [2] Wronski, Christopher R., and David E. Carlson. Chap. 5 *Amorphous silicon solar cells*. In *Clean Electricity from Photovoltaics*. Eds Archer MD and Hill R. Imperial College Press, London, UK, 2001.
- [3] A.V. Shah, H. Schade, M. Vanecek, J. Meier, E. Vallat-Sauvain, N. Wyrsh, U. Kroll, C. Droz, J. Bailat, Thin-film silicon solar cell technology, *Prog. Photovolt. Res. Appl.* 12 (2004) 113–142. doi:10.1002/pip.533.

- [4] D.L. Staebler, C.R. Wronski, Reversible conductivity changes in discharge-produced amorphous Si, *Appl. Phys. Lett.* 31 (1977) 292–294. doi:10.1063/1.89674.
- [5] Wronski, C.R., Pearce, J.M., Koval, R.J., Niu, X., Ferlauto, A.S., Koh, J. and Collins, R.W., 2002. Light induced defect creation kinetics in thin film protocrystalline silicon materials and their solar cells. In *MRS Proceedings*(Vol. 715, pp. A13-4). Cambridge University Press. doi: 10.1557/PROC-715-A13.4
- [6] Wronski, C. R., J. M. Pearce, J. Deng, V. Vlahos, and R. W. Collins. Intrinsic and light induced gap states in a-Si: H materials and solar cells—effects of microstructure. *Thin Solid Films* 451 (2004) 470-475. doi:10.1016/j.tsf.2003.10.129
- [7] H.W. Deckman, Optically enhanced amorphous silicon solar cells, *Appl. Phys. Lett.* 42 (1983) 968. doi:10.1063/1.93817.
- [8] R.E.I. Schropp, M. Zeman, Amorphous and microcrystalline silicon solar cells: modeling, materials, and device technology, Kluwer Academic, Boston, 1998.
- [9] M.A. Green, Solar cells: operating principles, technology, and system applications, Prentice-Hall, 1982.
- [10] J. Müller, B. Rech, J. Springer, M. Vanecek, TCO and light trapping in silicon thin film solar cells, *Sol. Energy.* 77 (2004) 917–930. doi:10.1016/j.solener.2004.03.015.
- [11] V.E. Ferry, M.A. Verschuuren, H.B.T. Li, E. Verhagen, R.J. Walters, R.E.I. Schropp, H.A. Atwater, A. Polman, Plasmonic light trapping for thin film A-Si:H solar cells, in: 2010 35th IEEE Photovolt. Spec. Conf. PVSC, 2010: pp. 000760–000765. doi:10.1109/PVSC.2010.5617101.
- [12] P. Spinelli, V.E. Ferry, J. van de Groep, M. van Lare, M.A. Verschuuren, R.E.I. Schropp, H.A. Atwater, A. Polman, Plasmonic light trapping in thin-film Si solar cells, *J. Opt.* 14 (2012) 024002. doi:10.1088/2040-8978/14/2/024002.
- [13] R.W. Collins, A.S. Ferlauto, G.M. Ferreira, C. Chen, J. Koh, R.J. Koval, Y. Lee, J.M. Pearce, C.R. Wronski, Evolution of microstructure and phase in amorphous, protocrystalline, and microcrystalline silicon studied by real time spectroscopic ellipsometry, *Sol. Energy Mater. Sol. Cells.* 78 (2003) 143–180. doi:10.1016/S0927-0248(02)00436-1.
- [14] R.J. Koval, J.M. Pearce, A.S. Ferlauto, R.W. Collins, C.R. Wronski, The role of phase transitions between amorphous and microcrystalline silicon on the performance of protocrystalline Si:H solar cells, in: *IEEE*, 2000: pp. 750–753. doi:10.1109/PVSC.2000.915992.
- [15] D. Derkacs, S.H. Lim, P. Matheu, W. Mar, E.T. Yu, Improved performance of amorphous silicon solar cells via scattering from surface plasmon polaritons in nearby metallic nanoparticles, *Appl. Phys. Lett.* 89 (2006) 093103. doi:10.1063/1.2336629.
- [16] H.R. Stuart, D.G. Hall, Island size effects in nanoparticle-enhanced photodetectors, *Appl. Phys. Lett.* 73 (1998) 3815. doi:10.1063/1.122903.
- [17] D.M. Schaadt, B. Feng, E.T. Yu, Enhanced semiconductor optical absorption via surface plasmon excitation in metal nanoparticles, *Appl. Phys. Lett.* 86 (2005) 063106. doi:10.1063/1.1855423.
- [18] K. Nakayama, K. Tanabe, H.A. Atwater, Plasmonic nanoparticle enhanced light absorption in GaAs solar cells, *Appl. Phys. Lett.* 93 (2008) 121904. doi:10.1063/1.2988288.
- [19] S. Mookapati, F.J. Beck, A. Polman, K.R. Catchpole, Designing periodic arrays of metal nanoparticles for light-trapping applications in solar cells, *Appl. Phys. Lett.* 95 (2009) 053115. doi:10.1063/1.3200948.

- [20] A. Vora, J. Gwamuri, J.M. Pearce, P.L. Bergstrom, D.Ö. Güney, Multi-resonant silver nano-disk patterned thin film hydrogenated amorphous silicon solar cells for Staebler-Wronski effect compensation, *J. Appl. Phys.* 116 (2014) 093103. doi:10.1063/1.4895099.
- [21] H.A. Atwater, A. Polman, Plasmonics for improved photovoltaic devices, *Nat. Mater.* 9 (2010) 205–213. doi:10.1038/nmat2629.
- [22] J. Gwamuri, M. Marikkannan, J. Mayandi, P. Bowen, J. Pearce, Influence of Oxygen Concentration on the Performance of Ultra-Thin RF Magnetron Sputter Deposited Indium Tin Oxide Films as a Top Electrode for Photovoltaic Devices, *Materials.* 9 (2016) 63. doi:10.3390/ma9010063.
- [23] J. Gwamuri, A. Vora, R.R. Khanal, A.B. Phillips, M.J. Heben, D.O. Güney, P. Bergstrom, A. Kulkarni, J.M. Pearce, Limitations of ultra-thin transparent conducting oxides for integration into plasmonic-enhanced thin-film solar photovoltaic devices, *Mater. Renew. Sustain. Energy.* 4 (2015). doi:10.1007/s40243-015-0055-8.
- [24] C.L. Haynes, R.P. Van Duyne, Nanosphere Lithography: A Versatile Nanofabrication Tool for Studies of Size-Dependent Nanoparticle Optics, *J. Phys. Chem. B.* 105 (2001) 5599–5611. doi:10.1021/jp010657m.
- [25] A. Kosiorek, W. Kandulski, H. Glaczynska, M. Giersig, Fabrication of Nanoscale Rings, Dots, and Rods by Combining Shadow Nanosphere Lithography and Annealed Polystyrene Nanosphere Masks, *Small.* 1 (2005) 439–444. doi:10.1002/sml.200400099.
- [26] C. Langhammer, Z. Yuan, I. Zorić, B. Kasemo, Plasmonic Properties of Supported Pt and Pd Nanostructures, *Nano Lett.* 6 (2006) 833–838. doi:10.1021/nl060219x.
- [27] C. Langhammer, M. Schwind, B. Kasemo, I. Zorić, Localized Surface Plasmon Resonances in Aluminum Nanodisks, *Nano Lett.* 8 (2008) 1461–1471. doi:10.1021/nl080453i.
- [28] E.M. Larsson, J. Alegret, M. Käll, D.S. Sutherland, Sensing Characteristics of NIR Localized Surface Plasmon Resonances in Gold Nanorings for Application as Ultrasensitive Biosensors, *Nano Lett.* 7 (2007) 1256–1263. doi:10.1021/nl0701612.
- [29] R. Morarescu, H. Shen, R.A.L. Vallée, B. Maes, B. Kolaric, P. Damman, Exploiting the localized surface plasmon modes in gold triangular nanoparticles for sensing applications, *J. Mater. Chem.* 22 (2012) 11537. doi:10.1039/c2jm30944k.
- [30] C. Battaglia, C.-M. Hsu, K. Söderström, J. Escarré, F.-J. Haug, M. Charrière, M. Boccard, M. Despeisse, D.T.L. Alexander, M. Cantoni, Y. Cui, C. Ballif, Light Trapping in Solar Cells: Can Periodic Beat Random?, *ACS Nano.* 6 (2012) 2790–2797. doi:10.1021/nn300287j.
- [31] J. Bhattacharya, N. Chakravarty, S. Pattnaik, W.D. Slafer, R. Biswas, V.L. Dalal, A photonic-plasmonic structure for enhancing light absorption in thin film solar cells, *Appl. Phys. Lett.* 99 (2011) 131114. doi:10.1063/1.3641469.
- [32] P.-Y. Chen, H.-H. Hsiao, C.-I. Ho, C.-C. Ho, W.-L. Lee, H.-C. Chang, S.-C. Lee, J.-Z. Chen, I.-C. Cheng, Periodic anti-ring back reflectors for hydrogenated amorphous silicon thin-film solar cells, *Opt. Express.* 22 (2014) A1128. doi:10.1364/OE.22.0A1128.
- [33] C. Pahud, V. Savu, M. Klein, O. Vazquez-Mena, F. Haug, J. Brugger, C. Ballif, Stencil-Nanopatterned Back Reflectors for Thin-Film Amorphous Silicon n-i-p Solar Cells, *IEEE J. Photovolt.* 3 (2013) 22–26. doi:10.1109/JPHOTOV.2012.2213583.
- [34] G. Tagliabue, H. Eghlidi, D. Poulidakos, Facile multifunctional plasmonic sunlight harvesting with tapered triangle nanopatterning of thin films, *Nanoscale.* 5 (2013) 9957–9962. doi:10.1039/C3NR03273F.

- [35] X. Fan, W. Zheng, D.J. Singh, Light scattering and surface plasmons on small spherical particles, *Light Sci. Appl.* 3 (2014) e179. doi:10.1038/lsa.2014.60.
- [36] C.F. Bohren, D.R. Huffman, eds., *Absorption and Scattering of Light by Small Particles*, Wiley-VCH Verlag GmbH, Weinheim, Germany, 1998. <http://doi.wiley.com/10.1002/9783527618156> (accessed June 1, 2016).
- [37] H. Mertens, A.F. Koenderink, A. Polman, Plasmon-enhanced luminescence near noble-metal nanospheres: Comparison of exact theory and an improved Gersten and Nitzan model, *Phys. Rev. B.* 76 (2007). doi:10.1103/PhysRevB.76.115123.
- [38] Y.A. Akimov, W.S. Koh, K. Ostrikov, Enhancement of optical absorption in thin-film solar cells through the excitation of higher-order nanoparticle plasmon modes, *Opt. Express.* 17 (2009) 10195. doi:10.1364/OE.17.010195.
- [39] T.H. Besseling, M. Hermes, A. Fortini, M. Dijkstra, A. Imhof, A. van Blaaderen, Oscillatory shear-induced 3D crystalline order in colloidal hard-sphere fluids, *Soft Matter.* 8 (2012) 6931–6939. doi:10.1039/C2SM07156H.
- [40] X. Yan, J. Yao, G. Lu, X. Li, J. Zhang, K. Han, B. Yang, Fabrication of Non-Close-Packed Arrays of Colloidal Spheres by Soft Lithography, *J. Am. Chem. Soc.* 127 (2005) 7688–7689. doi:10.1021/ja0428208.
- [41] S. Babar, J.H. Weaver, Optical constants of Cu, Ag, and Au revisited, *Appl. Opt.* 54 (2015) 477. doi:10.1364/AO.54.000477.
- [42] Daryl Myers, Keith Emery, Chris Gueymard, Revising and Validating Spectral Irradiance Standards for Photovoltaic Performance, (2002). doi:10.13140/2.1.3050.0487.
- [43] C. Langhammer, B. Kasemo, I. Zorić, Absorption and scattering of light by Pt, Pd, Ag, and Au nanodisks: Absolute cross sections and branching ratios, *J. Chem. Phys.* 126 (2007) 194702. doi:10.1063/1.2734550.
- [44] B. Luk'yanchuk, N.I. Zheludev, S.A. Maier, N.J. Halas, P. Nordlander, H. Giessen, C.T. Chong, The Fano resonance in plasmonic nanostructures and metamaterials, *Nat. Mater.* 9 (2010) 707–715. doi:10.1038/nmat2810.
- [45] U. Herr, B. Kuerbanjiang, C. Benel, G. Papageorgiou, M. Goncalves, J. Boneberg, P. Leiderer, P. Ziemann, P. Marek, H. Hahn, Near-field effects and energy transfer in hybrid metal-oxide nanostructures, *Beilstein J. Nanotechnol.* 4 (2013) 306–317. doi:10.3762/bjnano.4.34.
- [46] J. Butet, P.-F. Brevet, O.J.F. Martin, Optical Second Harmonic Generation in Plasmonic Nanostructures: From Fundamental Principles to Advanced Applications, *ACS Nano.* 9 (2015) 10545–10562. doi:10.1021/acs.nano.5b04373.
- [47] M. A. van der Veen, G. Rosolen, T. Verbiest, M.K. Vanbel, B. Maes, B. Kolaric, Nonlinear optical enhancement caused by a higher order multipole mode of metallic triangles, *J Mater Chem C.* 3 (2015) 1576–1581. doi:10.1039/C4TC02427C.
- [48] X. Chen, B. Jia, J.K. Saha, B. Cai, N. Stokes, Q. Qiao, Y. Wang, Z. Shi, M. Gu, Broadband Enhancement in Thin-Film Amorphous Silicon Solar Cells Enabled by Nucleated Silver Nanoparticles, *Nano Lett.* 12 (2012) 2187–2192. doi:10.1021/nl203463z.
- [49] L.J. Sherry, R. Jin, C.A. Mirkin, G.C. Schatz, R.P. Van Duyne, Localized Surface Plasmon Resonance Spectroscopy of Single Silver Triangular Nanoprisms, *Nano Lett.* 6 (2006) 2060–2065. doi:10.1021/nl061286u.
- [50] A. Mihi, M. Ocaña, H. Míguez, Oriented Colloidal-Crystal Thin Films by Spin-Coating Microspheres Dispersed in Volatile Media, *Adv. Mater.* 18 (2006) 2244–2249. doi:10.1002/adma.200600555.

- [51] Y. Fang, B.M. Phillips, K. Askar, B. Choi, P. Jiang, B. Jiang, Scalable bottom-up fabrication of colloidal photonic crystals and periodic plasmonic nanostructures, *J. Mater. Chem. C*. 1 (2013) 6031. doi:10.1039/c3tc30740a.
- [52] J.P. Hoogenboom, C. Rétif, E. de Bres, M. van de Boer, A.K. van Langen-Suurling, J. Romijn, A. van Blaaderen, Template-Induced Growth of Close-Packed and Non-Close-Packed Colloidal Crystals during Solvent Evaporation, *Nano Lett.* 4 (2004) 205–208. doi:10.1021/nl034867h.